



Absorbance measurement for in situ process regime identification in laser processing

Moritz Wittemer¹ · Jonas Grünewald¹ · Katrin Wudy¹

Received: 15 September 2022 / Accepted: 29 January 2023 / Published online: 22 February 2023
© The Author(s) 2023

Abstract

Laser melting can be conducted in two different process regimes, the conduction and the keyhole mode, which exhibit significantly different characteristics, dynamics, and stability and are highly sensitive to a magnitude of process parameters. Despite these differences and the resulting high relevance of the prevailing process regime for process development, the regime is commonly deduced after specimen testing. An identification of the regime parallel to the process could speed up the process development of, for example, laser beam welding or laser-based powder bed fusion of metals. Therefore, the possibility of an in situ regime identification under process-near conditions is the aim of these investigations. For this, the absorbance is measured in situ by using an integrating sphere on an in-house-developed test rig. This test rig can mimic real production process conditions to detect the characteristic change in the degree of absorption when switching between the process regimes. These measurements were conducted during experiments in which only the laser power was varied. A significant change in absorption was detected at a threshold laser power of 100 W, which correlates with the transition between the process regimes' conduction and keyhole regime. This threshold was proven by subsequent identification analysis of micrographic cross sections. This correlation promises the possibility of fast in situ process regime identification under near-real production process conditions with the potential of accelerating process development.

Keywords Laser material interaction · Conduction welding · Absorption · Integrating sphere · Keyhole

1 Introduction

The European Technology Platform Photonics21, which works closely together with the European Commission, predicts a bright future for the photonic industry and ushers in the twenty-first century as the “photon century” [1]. This statement is proven by the steadily increasing acceptance and maturity level of laser processing, such as laser beam welding (LBW) and laser-based powder bed fusion of metals (PBF-LB/M), in a variety of industries such as medicine,

aerospace, automotive, mobility, and electronics. Nevertheless, because of the sensitivity of the process in LBW and PBF-LB/M towards small changes in the process parameters, significant effort is required to optimize a laser process to the point of meeting all requirements of quality and reproducibility. One example of this sensitivity is the strong dependence of the prevailing process regime on the process parameters. This dependency is challenging during process development because the prevailing process regime strongly influences the process result. Two process regimes are distinguished in LBW and PBF-LB/M: heat conduction welding, also known as conduction mode, and deep penetration welding, also known as keyhole mode. Figure 1 provides a schematic illustration of a cross-section of the process zone during conduction and keyhole mode. In heat conduction welding, the laser power is absorbed on the surface of the material, and the resulting heat is conducted into the material. This limits the achievable aspect ratio of weld depth to width. In deep penetration welding, the radiation intensity exceeds the threshold for vaporizing the material. The vapor capillary funnels the laser radiation deeper into the material

✉ Moritz Wittemer
moritz.wittemer@tum.de

Jonas Grünewald
jonas.gruenewald@tum.de

Katrin Wudy
katrin.wudy@tum.de

¹ Professorship of Laser-based Additive Manufacturing, Department of Mechanical Engineering, School of Engineering & Design, Technical University of Munich, Boltzmannstraße 15, 85748 Garching, Germany

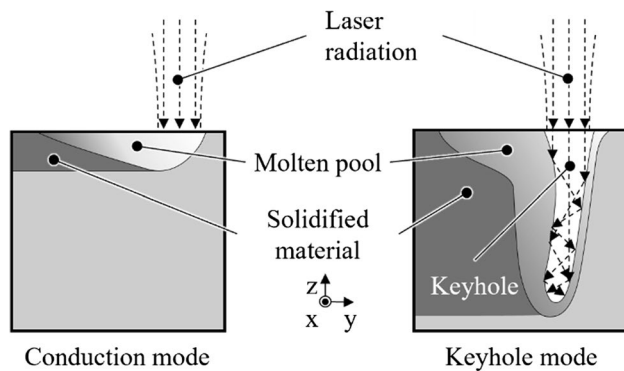


Fig. 1 Schematic cross-section of the process zone during welding in conduction and keyhole mode

and leads to multiple reflections, considerably increasing the degree of absorption, and the achievable aspect ratio is also significantly higher [2, 3].

These distinct differences have a significant impact on the process results. For example, in the case of LBW, a deep penetrating process might be required to form a significantly strong joint. A process in the conduction regime can lead to an insufficient weld depth, which can lead to weld failure under stress. In the case of PBF-LB/M, a keyhole process can lead to a porous part that exhibits insufficient mechanical properties [4–6].

The transition between these melting modes occurs at irradiation intensities of $1 \cdot 10^6 - 2 \cdot 10^6 \text{ W/cm}^2$ [3]. The distinct difference in the resulting aspect ratio of both process regimes is commonly used to identify the prevailing process regime. The aspect ratio threshold between conduction and keyhole mode varies in the literature between 0.8 and 1.0 [7–10]. But the distinction by aspect ratio can only be applied in the aftermath of the process via metallographic cross-sections, which necessitates an iterative and time-consuming approach of alternating experiments and specimen testing for the process development. This approach will reach its limits in the future because novel materials and processes, such as using different beam profiles, further multiply the available process parameters and, in turn, increase the number of iterations and time requirements. These novel techniques show great potential [11] and will require adjustment and optimization of existing processes to include these developments. Therefore, the identification of the prevailing process regime using in situ process monitoring instead of subsequent analysis can be highly beneficial for process development and optimization because it promises to significantly accelerate the procedure.

Currently, process monitoring is mainly focused on detecting individual defects and process characteristics [12, 13]. Common approaches include optical [14], acoustic [15], X-ray [16], pyrometric [17], and spectroscopical [18] techniques.

Even though all monitoring systems, which measure the temperature of the process zone, allow to indirectly deduce the laser absorption by determining the amount of absorbed energy, none of these techniques measure directly and in real-time the most fundamental feature of the different process regimes: the degree of absorption in the moment of irradiance. The investigated approach of a time-resolved absorption measurement is required for in situ process regime identification via absorption. This can be implemented by using an integrating sphere. With an integrating sphere, the absorption is calculated based on the reflection of the laser radiation during the process. The following examples show the application of an integrating sphere for in situ absorption measurement.

In 2008, Norris and Robino [19] presented an experimental setup based on two integrated spheres to explore the energy absorption for laser beam spot welds. The primary sphere detected the diffuse reflection of the material. Direct reflections were measured with the secondary sphere. The finding was the correlation between the different welding regimes and absorption values.

Simonds et al. [20] used a self-build set-up based on an integrated sphere to measure the absorption or the coupling efficiency during a 10 ms laser spot weld in 316L stainless steel. They proved the increase of the coupling efficiency on the boundary from the conduction to the keyhole welding regime. In [21], Simonds et al. compared the average absorption results from the prior investigations with calorimetric measured values. It was found that the direct calorimetric method underestimates the absorbed energy due to mass lost during a spot weld since direct measurement techniques such as laser calorimetry do not measure the laser absorption directly but rather measure the temperature increase of material after it has been illuminated by a laser [22]. Allen et al. [23] further equipped the integrated sphere set-up with a state-of-the-art real-time melt depth measurement technique. This optical coherence tomography confirms and explores the correlation between the highly dynamic vapor depression geometry in laser deep penetration welding and laser energy absorption.

The laser absorption in powder material is strictly different compared to solid material due to multiple reflections and the surface of the powder particles. In [24], Simonds et al. analyzed the optical coupling behavior of thin layers of stainless steel powder 316L. The key findings were the higher absorption of powder compared to solid materials. The dynamic behavior of the absorptance reveals physical phenomena, including oxidation, melting, and keyhole formation. Even for powder material, this keyhole formation includes an increase in absorption, as Trapp et al. demonstrated with direct calorimetric measurements [25]. Simultaneous measurements of laser power absorption and high-speed x-ray imaging were made to correlate time-resolved keyhole geometry with laser

energy absorption on laser welds of Ti6Al4V [26]. They investigated the periodic nature of absorptance, which was traced back to protrusions of the keyhole sidewalls that either narrowed the keyhole opening or reduced the overall keyhole area. These investigations were expanded to powder bed absorption measurements and simultaneous high-speed synchrotron imaging to transfer and conduct the results to powder bed fusion of Ti6Al4V [27]. The core finding is the strong correlation between laser absorption and the stability of the vapor depression. Simonds et al. [27] found a significant laser absorption reduction due to a change in the vapor depression aspect ratio, an event that is correlated to the formation of porosity. A 1070 nm and 1 kW Yb-doped fiber laser was used at a spot size of 49.5 μm for all the investigations.

These examples show the possibility of detecting the threshold between conduction and keyhole process regime by its characteristic change in the degree of absorption via an absorbance measurement. This threshold has only been detected by finely calibrated systems and extensive knowledge and control of the process conditions. The introduced approaches are not suitable at this point to significantly reduce the effort of process development and are often not applicable under near-process conditions.

Therefore, this paper investigates the possibility of detecting the prevailing process regime in situ under real processing conditions without necessitating calibration or prior knowledge of the processed material or conditions. For this, an experimental set-up based on an integrating sphere is used, which facilitates automated in situ data logging and spatial mapping of the integrating sphere signal. These data are analyzed for the characteristic change of the degree of absorption to identify the threshold between conduction and keyhole mode. The identified threshold is validated by evaluating micrographic cross-sections of the test specimens. In the future, a transfer of the developed method to different dosage forms is planned, such as powders for powder bed fusion and varying materials.

2 Materials and methods

2.1 Experimental set-up

An in-house-developed test rig was used for the experiments. The test rig is equipped with a fiber laser of the type *nLIGHT* AFX-1000 with a wavelength of 1070 nm. The laser is focused and guided by a *RAYLASE* AM-MODULE. This scanner optic is equipped with two independent *z*-axes, which facilitate a variable choice of laser spot diameter at a constant focal length. Caustic measurements, conducted according to DIN EN ISO 11146, yielded a spot diameter of $d_s = 93 \mu\text{m}$ for the applied scaling factor of one. The measured intensity distribution is visualized in Fig. 2.

The laser radiation hits the test specimen surface at an angle of incidence between $+0.9^\circ$ and -0.9° to the surface normal for all experiments. The focal plane is positioned on the specimen's surface.

A cross jet is mounted to the system to produce a strong airflow between the test specimen and the sphere. Thus, contamination of the sphere's inner surface by oxides and the influence of the weld plume on the measurement is mitigated.

2.2 Measurement system

The employed measurement system consists of two photodiode sensors. One diode is fiber coupled to an integrating sphere, and the second diode is integrated into the laser source. The signals will be referred to as integrating sphere signal and back-reflection signal, respectively. During the experiments, the incident laser radiation is partially reflected and absorbed at the target. A portion of the off-normal scattered reflected radiation dissipates to the sides, and one portion is captured by the integrating sphere. The sphere consists of two additively manufactured PA12 halves with an inner diameter of $d_{\text{Sphere}} = 120 \text{ mm}$ and two opposite apertures in line with the laser propagation with diameters of $d_{A1} = 15 \text{ mm}$ and $d_{A2} = 30 \text{ mm}$.

The inner surface of the sphere is coated with multiple layers of barium sulfate (BaSO_4) to create a Lambertian surface. Therefore, the captured radiation is distributed homogeneously by multiple reflections within the sphere to an average intensity. This resulting radiation is coupled into a fiber, which is shielded by a baffle to the process zone to block the direct line of sight. At the end of the fiber, the wavelength of the laser is isolated by a 1070 nm bandpass filter and focused on a switchable-gain photodetector (Thorlabs PDA100A2).

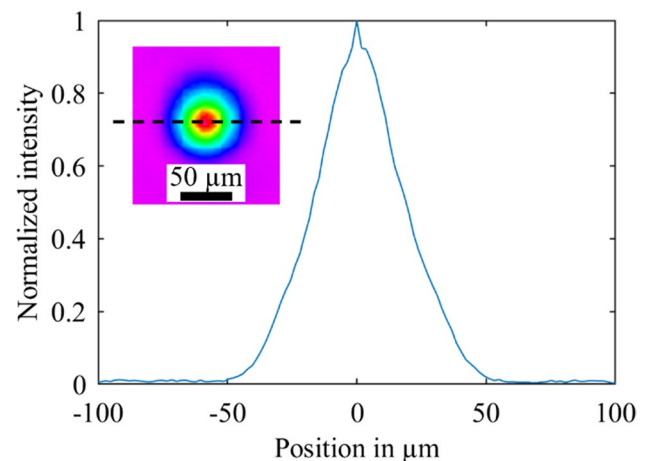


Fig. 2 Normalized intensity distribution at the focus distance of the employed setup

The sphere is mounted at a distance of $l_{\text{distance}} = 20$ mm to the target. A principal illustration of the system is shown in Fig. 3.

Within the laser, the directly reflected light is monitored by default to facilitate an emergency shutdown in case of an excessive amount of back-reflection, which might damage the system. The analog signal from this back-reflection sensor and the integrating sphere diode are sampled at a frequency of $f_M = 20$ kHz by the programmable logic controller (PLC) of the test bench. The laser itself updates its outgoing back-reflection signal at a rate of 10 kHz, which leads to a change of the signal in the data every two measuring points. This facilitates a simultaneous triggering of the emission and the data logging and gives access to metadata of the process, allowing a temporal and spatial mapping of the sensor data to the melt tracks during the data processing.

Conditioned by the geometric setup of the sphere, only partial monitoring of the reflected radiation is possible because the portion radiating past the sphere is not considered. Due to this unknown portion of reflected radiation, it is not possible to calculate the absorption directly from the reflection, even though the transmitted power is eliminated from the power equation for AISI 316L at this thickness. This leads to qualitative absorption information based on a qualitative reflection measurement.

2.3 Test specimens

The samples are cut out of a hot-rolled, 5 mm thick AISI 316L sheet. The surface of the test specimens is sandblasted with corundum. This results in a reproducible dull surface finish, mitigating the influence of changing surface roughness on the absorptivity of the specimen. The test surface of the test specimens was degreased with isopropanol in advance to the experiments.

2.4 Job design and process parameters

Every experiment consists of $n_{\text{track}} = 49$ parallel melt tracks produced in direct succession at a distance of

$h = 200$ μm and a length of $l = 10$ mm, as seen in Fig. 4. Based on the jump speed of the scanner optic, the time between melt tracks was > 2 ms.

For all experiments, the scan speed v_{scan} is 500 mm/s and the laser power P_{Laser} is varied as listed in Table 1.

This means every experiment contains all measuring points of the 49 melt tracks in one test, which are produced with the same process parameters.

In this approach, the influence of the laser power on the process and, in turn, the measurement is isolated. The parameter space was selected based on the findings of Trapp et al. [25] because the transition from conduction to the keyhole process regime is to be expected for this increase in power. Their experiments were conducted on a similar laser set-up with the same material but a smaller spot diameter of 60 μm . Their experiments showed a transition between conduction and keyhole mode between 75 and 250 W. This means a transition between the melting modes occurs from a mean intensity of $I_{\text{mean,Trapp,min}} \approx 2.6 \cdot 10^6$ W/cm² to $I_{\text{mean,Trapp,max}} \approx 8.8 \cdot 10^6$ W/cm², which can be calculated by $I_{\text{mean}} = 4P_{\text{Laser}}/d_s^2 \cdot \pi$ with the spot diameter of 60 μm and a laser power of 75 and 250 W. The additional buffer up to 600 W in the selected parameters should accommodate the threshold despite the lowered intensity due to the larger spot size because with the selected parameters a comparable intensity span from a minimal mean intensity of $I_{\text{mean,min}} \approx 1.5 \cdot 10^6$ W/cm² at 100 W to a maximum mean intensity of $I_{\text{mean,max}} \approx 8.8 \cdot 10^6$ W/cm² at 600 W is reached with the spot size of 93 μm .

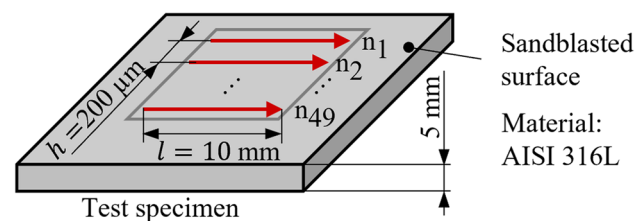


Fig. 4 Layout of the job design with melt track length, orientation, and test specimen information

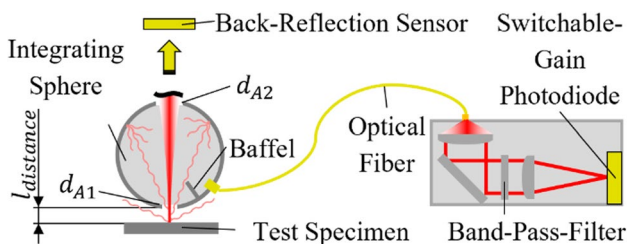


Fig. 3 Schematic illustration of the integrating sphere measurement system

Table 1 Process parameters for all considered experiments

Experiment	P_{Laser}
1	100 W
2	200 W
3	300 W
4	400 W
5	500 W
6	600 W

2.5 Melt track and micrograph images

The micrographs were prepared to evaluate the weld track width w_w and depth δ_w by cross-cutting the test specimens in the post-process. The cut-outs are embedded in a transparent epoxy, wet ground in three stages using silicon carbide paper (grit 180, 360, and 1200), and polished in two stages using polishing pastes (3 and 1 μm). Finally, the specimens are etched with an Adler etchant. The cross-section images are taken of eight melt tracks with an optical microscope. These images are used to determine the weld depth δ_w and the weld width w_w for each, as seen in Fig. 5. Afterward, the aspect ratio of these dimensions is calculated for each analyzed melt track and deducted to an arithmetic mean and a standard deviation of the aspect ratio with the formula from Fig. 5 for every laser power level.

Additionally, high-resolution images of every experiment’s melt tracks are taken to investigate the melt track surfaces and evaluate the homogeneity of the appearance. The images were taken with a Keyence VR-3000 at 80 \times magnification.

2.6 Data logging and processing

The logging of the constant data stream from the integrating sphere and the back-reflection signal during one experiment is interrupted at the end of every melt track, creating a separate data section per melt track. The constant sampling rate results in n_{points} measuring points and spacing $l_{\Delta P}$ of the measuring points, given by the equations:

$$n_{points} = \frac{l \cdot f_M}{v_{scan}}, l_{\Delta P} = \frac{l}{n_p}$$

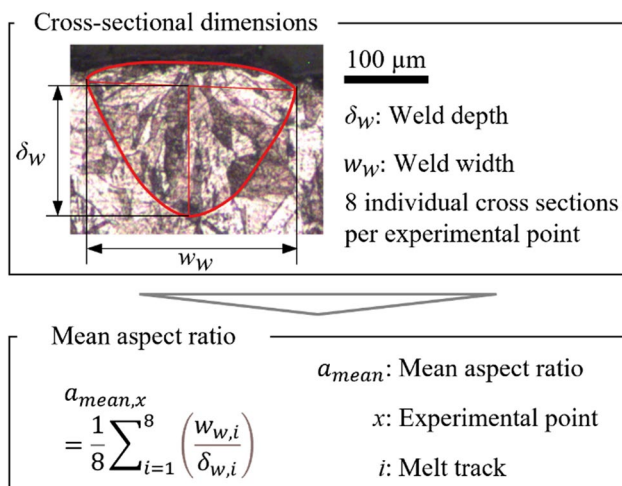


Fig. 5 Illustrated deduction of the cross-sectional weld depth dimension and calculation of the average aspect ratio

The resulting raw data from the data logging sequence of every experiment are a two-layered matrix. One layer contains the integrating sphere signal, and one the back-reflection signal. The data of every melt track are saved in a separate matrix line, resulting in a matrix with the following dimensions: $n_{track} \cdot n_{Points} \cdot 2$, which is schematically visualized in Fig. 6 (a) and represents the starting point of the data processing. The data processing procedure is conducted analog for the back-reflection and integrating sphere signal data.

Processing step 1 The first data processing step is the spatial mapping of the data. The data separation of every melt track in combination with the equidistant distribution of the measuring points over the length of the melt track and the constant distance of the melt tracks to each other facilitates a spatial mapping of the data to the process. The three-dimensional visualization of the spatially mapped data is exemplarily shown in Fig. 6 (b) for the integrating sphere signal at 500 W. The x - and y -axis correspond to the plane of the melt tracks, indicating the melt track and the position a measurement is taken on this melt track. The z -axis visualizes the measured intensity of the integrating sphere signal at this point. The color gradient additionally visualizes the intensity of the signal to conserve the information when the plot is analyzed in the top view on the x - y -plane.

The exemplary displayed integrating sphere signal at 500 W exhibits, as well as any other experiment, an initial signal peak and concluding drop at the beginning and end of every melt track. An approximately even surface forms in between the measuring points, which is intermittent by isolated and distinct signal peaks.

The spatially mapped data facilitates the data examination for possible correlation of signal and melt track features. To compare the data of one experiment to others and examine the trend over multiple experiments, spatial mapping must be abandoned. The data must be compressed by statistical description with a central tendency and spread, limiting the loss of information at the same time. This allows for the simultaneous display of multiple experiments in one visualization.

The evenness of the intermittent surface, which is observable in all experiments, indicates no significant interference for consecutive melt tracks by the change of the thermal balance within the test specimen or the surface structure by the previous melt track. Therefore, constant conditions for all melt tracks can be assumed.

Processing step 2 The continuity within one melt track and between individual melt tracks allows, in the second processing step, the collapse of data from all melt tracks to one data stream along the length of a melt track. The result is seen in

Fig. 6 Visualization of the four-step data processing procedure comprised of the spatial mapping (processing step 1) (b), combining to two dimensions (processing step 2) (c), trimming (processing step 3) (d), and collapsing to dimensionless point cloud (processing step 4) (e), starting with the raw data of one experiment (a)

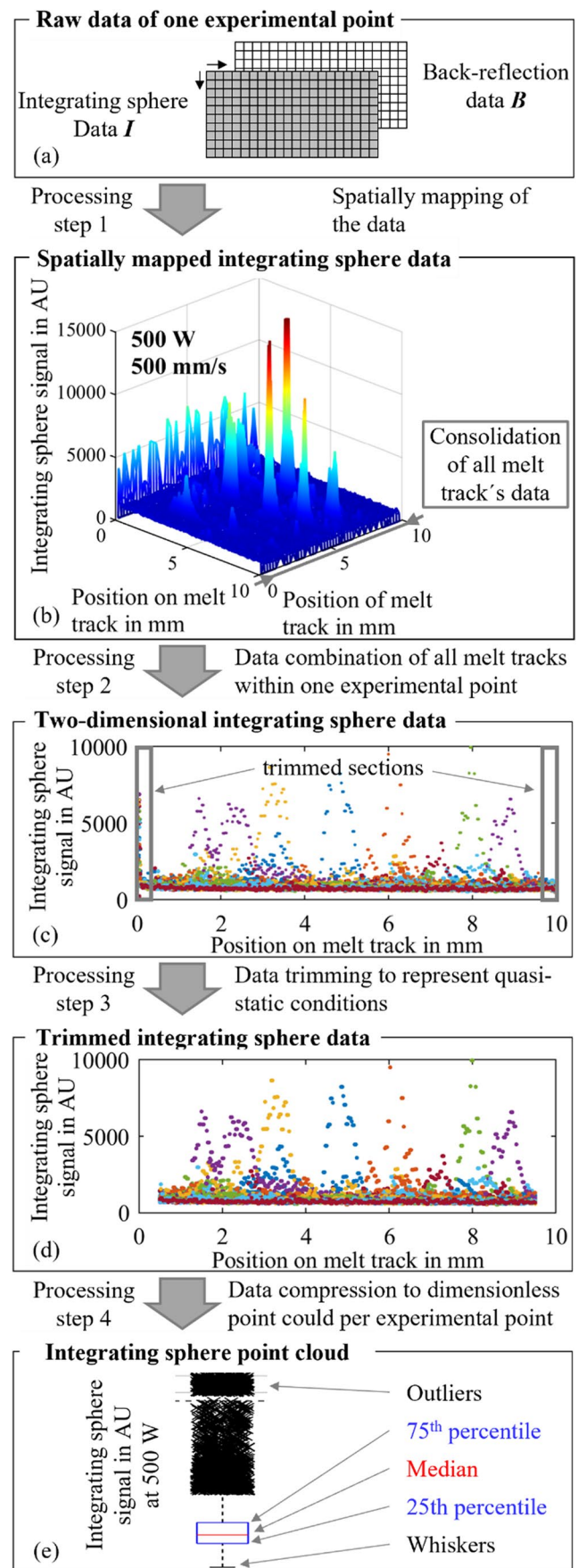
Fig. 6 (c), again exemplary for the integrating sphere signal at 500 W.

Processing step 3 The initial peak of the integrating sphere signal at the beginning of every melt track corresponds to the reflection of the laser radiation on the mirror-like surface of molten material. This phenomenon was also observed by Yang et al. [28]. This condition is a temporary occurrence during the ramping-up of the laser power and is not representative for the rest of the melt track. The same applies to the end of the melt track, where a drop in the signal corresponds to the emission cut-off. Thus, the first and last 5 % of measuring points of every melt track are cut off in the third processing step.

This results in the collection of data points displayed in Fig. 6 (d). All remaining measuring points were taken under the same quasi-static conditions. This suggests that the remaining isolated signal peaks are the result of process-related irregularities and are an indicator to evaluate the process. Therefore, all remaining measuring points represent the parameter-specific process.

Processing step 4 In the fourth processing step, all remaining measuring points are collapsed along the length of the melt track to one point cloud, which represents the measurement of one experiment. A statistical description of the point cloud facilitates the comparison of multiple experiments with one another by reducing them to one-dimensional statistical values of a tendency and spread. The comparison facilitates concluding the influence and correlation of process parameter changes on the signal changes. This statistical description of the point cloud is visualized by a boxplot in Fig. 6 (e) containing five features.

- The central red line represents the median of the measurement. The robustness of the median towards outliers results in a close relationship between the median value and the average signal value of the intermittent surface, spanned by the majority of the measuring points.
 - A decrease/increase of the median because of a process parameter change indicates a decrease or increase in the degree of the absorption during the process.
- The upper and lower limit of the blue box, enclosing the red line, mark the 25th and 75th percentiles of the



data. Thus, the box represents the interquartile range, indicating the spread of 50 % of the data in proximity to the median.

→ The box size indicates the stability of the signal and thereby indicates the reliability of the data.

- The whiskers incorporate all measuring points with a value smaller than 2 times the interquartile range. This provides more detail about the spread of the point cloud around the median.

→ The extent of the whiskers is a further indicator of the reliability, analog to the percentile range. Additionally, it visualizes the boundary to the classification of measuring points as outliers.

- The “x’s” mark all remaining points not incorporated by the whiskers as outliers, indicating a significant divergence from the median. All outliers marked in the width of the box belong to the same experiment. The spread over the entire width facilitates a superior estimation of the number of outliers.

→ A decrease or increase in the number of outliers indicates a change in the frequency of irregular signal peaks.

- All outliers above a certain maximal value, in this case, 2000, are compressed to a valueless section. For these outliers, their values are not visible and cannot be interpreted. Due to the qualitative assessment of the data, the focus is on the number of outliers and not their value.

→ Allows the focus of the value domain on the median range without forgoing the information on the outlier frequency.

The four processing steps are conducted for the integrating sphere and back-reflection data of all experiments. The results are shown in Fig. 7.

3 Results and discussion

3.1 Influence of laser power on the integrating sphere and back-reflection signal

For the integrating sphere data shown in Fig. 7 (a), this reveals an initial drop of the median between 100 and 200 W, followed by a plateau section up to 500 W and a rise of the median at 600 W. The number as well as the value of the outliers does not significantly change between 100 and 300 W. At 400 W, the number of outliers starts to increase, and for 500 and 600 W, the number and reach of the outliers is considerably higher.

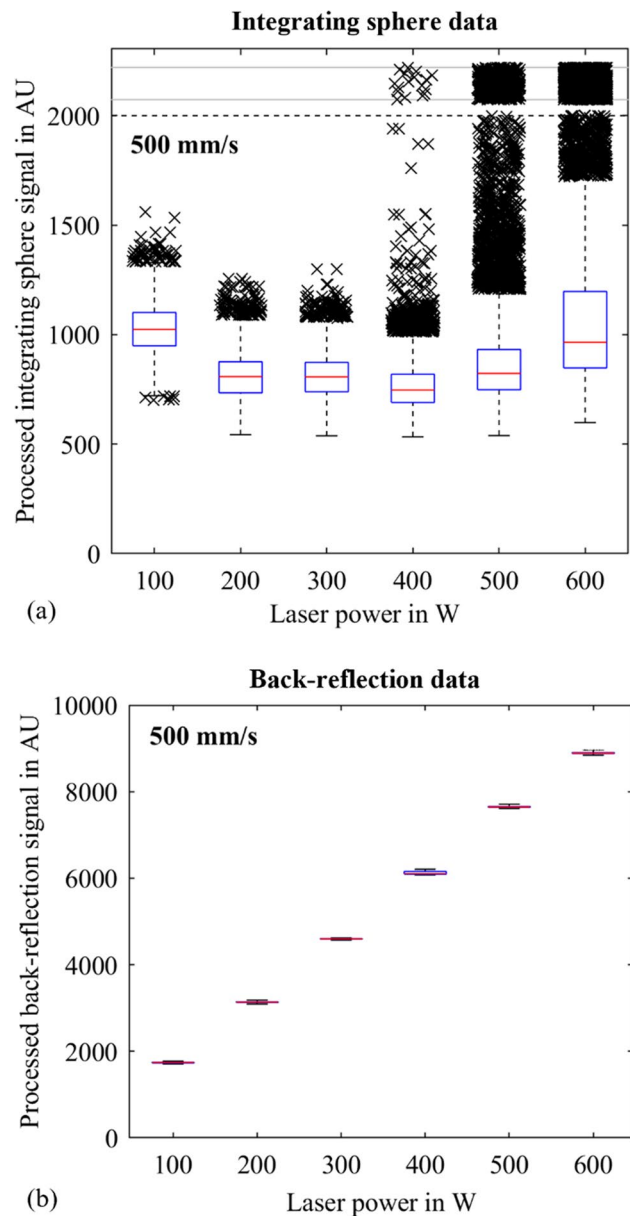


Fig. 7 Boxplot of the processed integrating sphere data (a) and corresponding back-reflection data (b) at 100–600 W and 500 mm/s

The lack of outliers from 100 to 300 W means that for these experiments, the data surface is not intermittent by isolated peaks, as is the case for 500 W, but shows an even surface. The integrating sphere data show different characteristics at different laser powers, indicating a change in the process behaviors with increasing laser power.

The back-reflection signal, shown in Fig. 7 (b), exhibits a highly stable behavior within each power level, visible by the lack of outliers and the non-visible reach of the whiskers. The median trend over increasing laser power displays a linear gradient from 100 to 600 W.

The comparison of the integrating sphere signal and the back-reflection signal demonstrates no matching characteristics, indicating no link between both signals. While the integrating sphere signal changes with the process behavior, the back-reflection signal is not influenced by the process. The sole observable connection of the back-reflection signal is with the laser power. This suggests a small internal reflection within the optical path of the scanner optic as the source of the signal. This is additionally supported by preliminary experiments with targets of different reflectivity, which had a great influence on the integrating sphere signal and no effect on the back-reflection signal.

3.2 Referenced absorption measurement

The integrating sphere signal trend of Fig. 7 (a) is the result of two factors: on the one hand, the process-specific absorption level, which is influenced by a plurality of factors such as material, surface texture, process regime, and properties of the laser radiation; on the other hand, the increase in laser power, which necessarily leads to an increase of measured reflection at a constant absorption level. To evaluate the influence of process parameters on the absorption level without absolute reflection values, the influence of rising laser power must be deducted. This is achieved by referencing the integrating sphere data trend to the change in output power. The back-reflection signal is analyzed to monitor the change in output power.

The following example illustrates the need for referencing the signal to the output power and the applied procedure. Without referencing the change in output power, a doubling of the laser power at a constant degree of absorption results in twice the absolute reflected radiation. To analyze the change in the degree of absorption, the reflection must be evaluated relative to the input power. This means when the input power is doubled, the reflection signal must be cut in half to represent the degree of absorption. Generalizing this concept and substituting the input power by the back-reflection results in the division of the integrating sphere signal by the corresponding back-reflection.

Figure 8 provides an overview of the referencing procedure. One arbitrary experiment serves as the baseline E_{Base} consisting of the integrating sphere data I_{Base} and the back-reflection data B_{Base} . Every experiment E_x of one examined test series is referenced to this baseline, resulting in the referenced experiments $E_{x,Ref}$ in two steps. The experiment E_{IP} , which is referenced, will be referred to as the experiment in process, consisting likewise of the integrating sphere signal data I_{IP} and the back-reflection data B_{IP} :

First referencing step In the first step the change, x_{change} , of the back-reflection signal between the baseline and the experiment in process is determined by comparing the respective back-reflection medians. This change is quantified

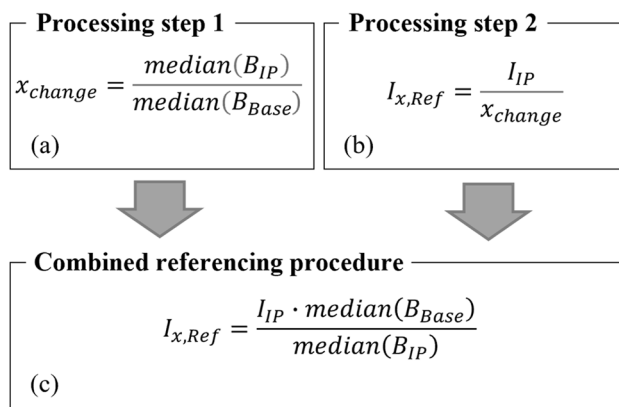


Fig. 8 Isolated processing steps one (a) and two (b) and the combined processing procedure (c)

by the division of the experiment in the process’ median (B_{IP}) by the baseline’s median (B_{Base}), as seen in Fig. 8 (a).

Second referencing step The second step is the actual referencing step. For this, the integrating sphere data in process I_{IP} are adjusted regarding the change of the back-reflection signal. For example, if the value of the back-reflection median doubles compared to the baseline, the integrating sphere signal is divided by two. The calculation is shown in Fig. 8 (b). The two referencing steps are combined into the calculation below, seen in Fig. 8 (c).

This referencing procedure is performed with all experiments of Fig. 7 (a), $E_{100\text{ W}}$ to $E_{600\text{ W}}$, with $E_{100\text{ W}}$ as a baseline, resulting in the plot in Fig. 9.

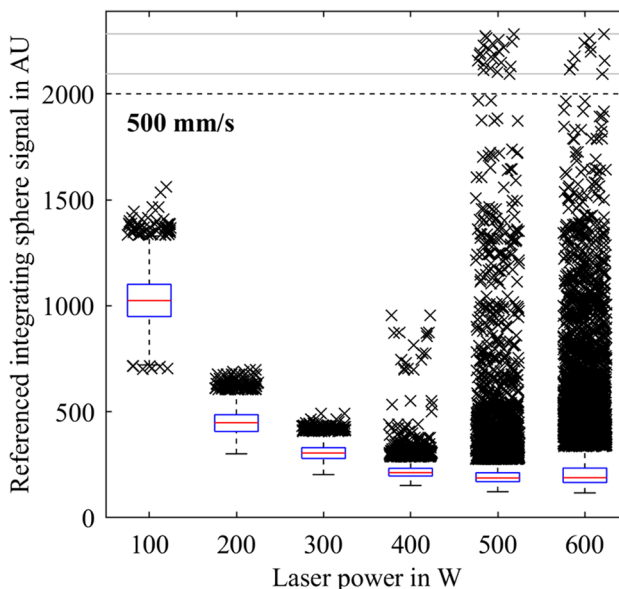


Fig. 9 Boxplot of referenced integrating sphere data for 100 to 600 W at 500 mm/s

The referenced data show the following characteristics: the outliers exhibit qualitatively the same distribution as for the unreferenced data with low occurrence up to 300 W, more at 400 W, and significantly more at 500 and 600 W. The median trend changes significantly, concerning the unreferenced data, exhibiting a considerable drop in value between 100 and 200 W, which continues with decreased magnitude until 400 W. From 400 to 600 W, the median plateaus.

Despite the isolation of the degree of absorption change over a change in laser power, identifying the threshold between conduction and keyhole mode is not possible. For this, the threshold must be linked to a feature of the median trend. This means that the threshold must be at first independently identified based on the test specimens. The micrograph images were analyzed for this.

3.3 Influence of the laser power on the melt track cross-section dimensions

For the evaluation of the prepared micrograph images, the arithmetic mean and the corresponding standard deviation of the width and depth are calculated over all evaluated cross-sections for each power level. The measurement positions of the melt track dimensions are marked exemplarily in Fig. 5, and the resulting dimensions are plotted in Fig. 10.

The average width demonstrates a continuous small increase from 100 to 400 W and remains at this width with small margins between 400 and 600 W. The depth increases significantly near-linearly between 100 and 500 W and further to 600 W with a smaller gain. The variation of the width and depth within a power level is small for 100 to 400 W, as the standard deviation shows. For 500 and 600 W, the standard deviation of the width is slightly higher and significantly higher for the depth.

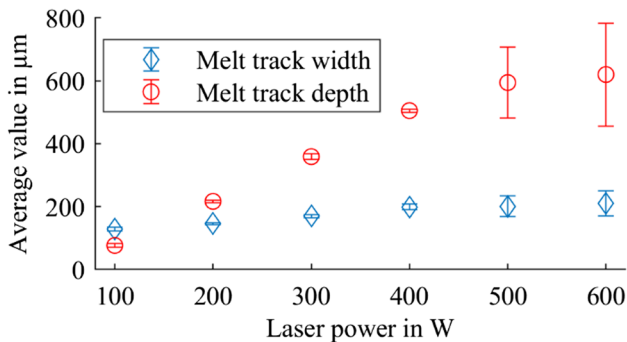


Fig. 10 Average melt track width and depth and corresponding standard deviation of the melt track cross sections produced by 100–600 W at 500 mm/s

For all power levels, the resulting average aspect ratio a_{mean} between the width and depth of the melt track is calculated, together with the corresponding standard deviation, with:

$$a_{\text{mean},x} = \frac{1}{7} \sum_{i=1}^7 \left(\frac{w_{w,i}}{\delta_{w,i}} \right)$$

The results are displayed in Fig. 11 with the laser power on the x -axis and the aspect ratio on the y -axis. The average aspect ratio of the melt tracks exhibits increasing values with small standard deviations from 100 to 500 W. To 600 W, the average aspect ratio increases insignificantly. The standard deviations remain small from 100 to 400 W but are significantly higher for 500 and 600 W.

The aspect ratio of the melt track dimensions is a decisive identifier of the prevailing process regime of the linked process. According to Tenbrock et al. [7], the threshold between conduction and keyhole mode is set at an aspect ratio of 0.8. Gan et al. [8], Helm et al. [9], and Fabbro [10] et al. set the threshold to an aspect ratio of 1. The resulting threshold zone is marked in Fig. 11, indicating a conduction process regime for the process at 100 W and a keyhole process regime for 200 to 600 W. Based on these power levels, a transition between conduction and keyhole mode occurs at a mean intensity of $I_{\text{mean,trans}} = 2.2 \cdot 10^6 \text{ W/cm}^2$. The comparison of the resulting $I_{\text{mean,trans}}$ with the transition intensities of Poprawe [3] with 1–2 W/cm^2 and Trapp et al. [25] with 2.6 W/cm^2 shows a similar magnitude of these values. Nevertheless, the discrepancy of those values, which is based on the unique conditions of every individual test series, makes the importance of an in situ threshold detection clear.

3.4 Correlation of degree of absorption and process regime

Figure 12 combines the results from the micrograph evaluation and the referencing of the integrating sphere signal. The

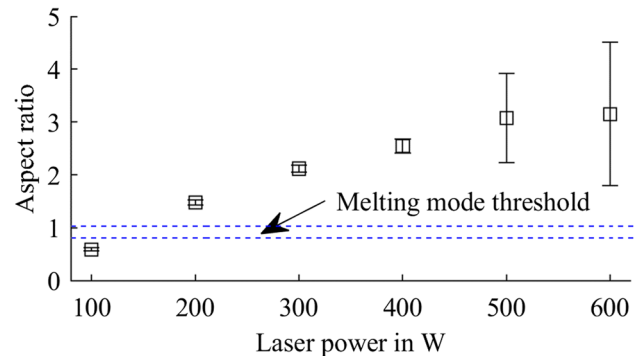


Fig. 11 Average aspect ratio of melt track width and depth with marked process regime threshold and the corresponding standard deviation for the experiments of Fig. 7

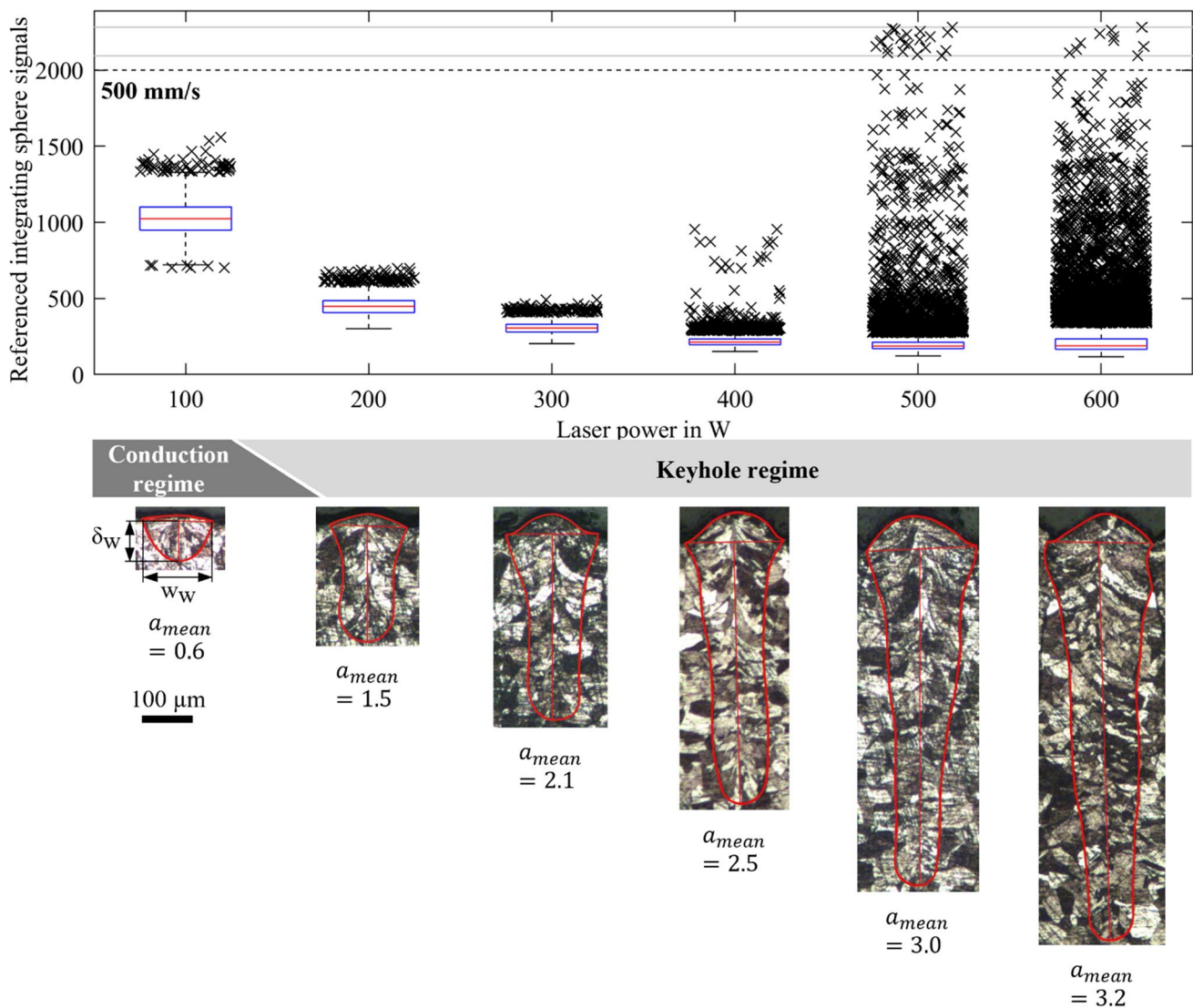


Fig. 12 Combined visualization of the reference integrating sphere boxplot at the top, the assignment of the parameter-specific prevailing process regime in the middle, and corresponding exemplary micrograph images at the bottom for 100 to 600 W at 500 mm/s

assignment of the processes at different laser power levels to the prevailing process regime, which is based on the aspect ratio of the resulting melt track, is shown below the boxplot of the referenced integrating sphere signal.

This reveals that the significant reduction of the referenced integrating sphere signal coincides with the transition from conduction to the keyhole mode. This supports the established model of a significant increase in the absorption level [2, 3] when entering the keyhole mode, which corresponds to a decrease in the reflected laser radiation. This in turn has a decreasing effect on the integrating sphere signal. The drop of the integrating sphere signal is significant compared to the signal spread within one experiment and the overall median trend over increasing laser power.

This demonstrates the possibility to identify the threshold between conduction and keyhole process regime by the means of a calibration-less, integrating-sphere-based in situ measurement.

3.5 Correlation of surface irregularities and integrating sphere signal peaks

As mentioned in the data processing section, the spatially mapped integrating sphere signal can be used to investigate the data for the local correlation of signal and melt track features. For this investigation, the spatially mapped integrating sphere signal, viewed from the z -direction, is set next to a high-resolution image of the corresponding melt

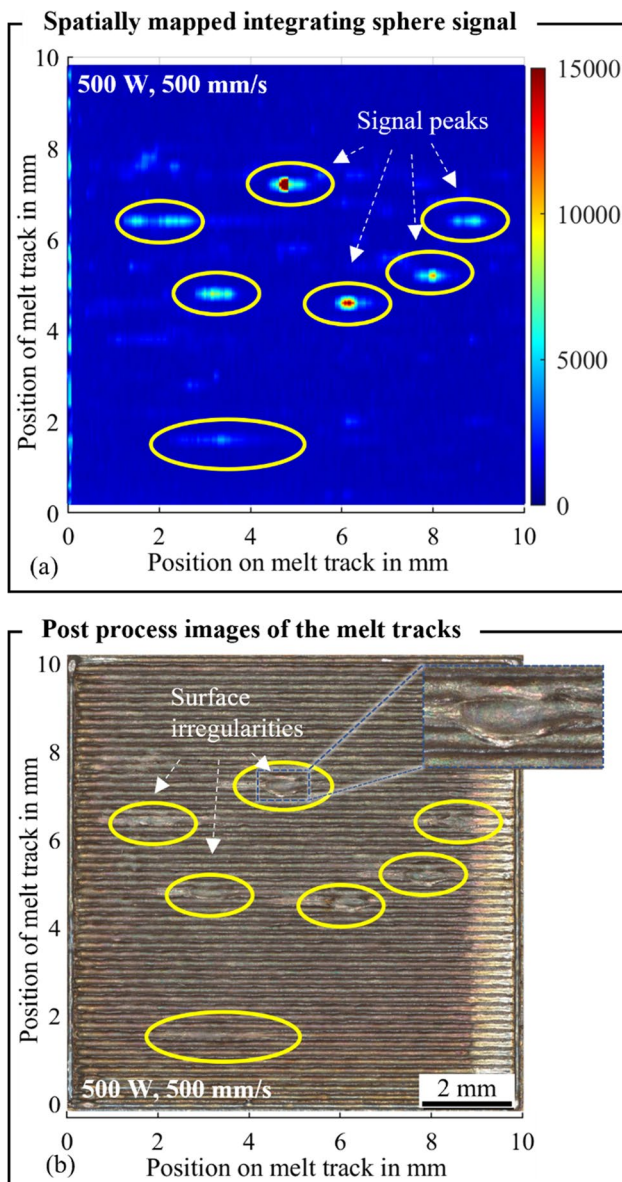


Fig. 13 Example of visible correlation (marked in yellow) between integrating sphere signal peaks and surface irregularities for 500 W and 500 mm/s

tracks. This visualization is exemplary given in Fig. 13 for the experiment at 500 W and 500 mm/s.

The figure displays an example of a spatial correlation of isolated signal peaks in the integrating sphere signal and visible surface irregularities. This correlation can be observed for all experiments exhibiting isolated signal peaks. Considering experiments in Sect. 3.1, these correlations are observable at 500 and 600 W. The visible surface irregularities at 500 and 600 W coincide with the significantly higher standard deviation of the melt track depth, discussed in Sect. 3.3, at the same power levels.

The higher variation of the melt track depth suggests a lower process stability, which is represented in the data by several signal peaks and, in turn, by a higher number of outliers in the compressed data. This links an exceptionally high occurrence of outliers as an in situ indicator to depressed process stability.

4 Conclusion and outlook

In this work, bead-on-plate welds were conducted on 316L stainless steel at different laser power levels to investigate the possibility of identifying the threshold between conduction and keyhole melting mode in situ using an integrating sphere without calibrating the measurement. To this end, the raw data were processed to allow spatial mapping of the signal to the process and, on the other hand, simultaneous visualization of multiple experiment data without a significant loss of information. Furthermore, to isolate the influence of the process dynamic on the integrating sphere signal from the influence of the increase in laser power, the signal was indirectly referenced to the output power by facilitating the back-reflection signal of the laser. Additionally, the resulting melt track dimensions were evaluated with cross-sectional micrograph images. Based on the discussion of the referenced integrating sphere signal and the micrograph analysis, the following conclusions were made about the integrating sphere-based process monitoring with AISI 316L:

- The spatial mapping of the integrating sphere signal to the melt tracks facilitates the targeted investigation of correlations between signal characteristics and melt track features. This is shown by the correlation between prominent peaks of the integrating sphere signal and visible surface irregularities in the melt track.
- The process stability can be assessed based on the integrating sphere signal since there is a link between the volatility of the signal and the stability of the weld depth, as well as the homogeneity of the melt track appearance.
- The threshold between conduction and keyhole process regime can be identified by a significant drop in the signal of the referenced integrating sphere signal. This signal decrease correlates with a change in the aspect ratio of the melt track associated with a change in the process regime.
- The above-listed conclusions were drawn from data that were acquired without preceding calibration steps and did not require any diligence during the experiment setup or execution. This robust measuring system facilitates, together with automated data logging and processing, high-throughput experiments.

For these reasons, the in situ process analysis of laser-based material processing with the introduced measuring system shows great potential to investigate the laser-material interaction for a magnitude of different materials and laser intensity levels and distributions. This can help to speed up the development of tailored process strategies for specific applications and materials. Another application of the in situ measurement is real-time feedback on the current process regime, which can be facilitated for real-time process monitoring and eventually real-time process control. Therefore, further experiments should investigate the transferability of these results onto different materials and the influence of change in the radiation intensity and distribution on the process regime threshold.

Author contribution Conceptualization: M.W. and K.W.; experimental set-up: M.W. and J.G.; data curation: M.W.; formal analysis: M.W.; micrographs: J.G. and M.W.; investigation: M.W.; methodology: M.W. and K.W.; project administration: M.W. and K.W.; funding: no additional/external funding was received for conducting this study; resources: K.W.; software: M.W.; supervision: M.W. and K.W.; validation: M.W.; visualization: M.W.; writing—original draft: M.W.; writing—review and editing: M.W. and K.W.

Funding Open Access funding enabled and organized by Projekt DEAL.

Data availability The data presented in this study are available on request from the corresponding author. The data are not publicly available as a result of ongoing research in this field.

Code availability The code used for data analysis is available on request from the corresponding author. The code is not publicly available as a result of ongoing research in this field.

Declarations

Ethics approval Not applicable.

Consent to participate Not applicable.

Consent for publication All authors have read and agreed to the published version of the manuscript.

Conflict of interest The authors declare no competing interests.

Open Access This article is licensed under a Creative Commons Attribution 4.0 International License, which permits use, sharing, adaptation, distribution and reproduction in any medium or format, as long as you give appropriate credit to the original author(s) and the source, provide a link to the Creative Commons licence, and indicate if changes were made. The images or other third party material in this article are included in the article's Creative Commons licence, unless indicated otherwise in a credit line to the material. If material is not included in the article's Creative Commons licence and your intended use is not permitted by statutory regulation or exceeds the permitted use, you will need to obtain permission directly from the copyright holder. To view a copy of this licence, visit <http://creativecommons.org/licenses/by/4.0/>.

References

1. VDI Technologiezentrum GmbH Europe's age of light!: how photonics will power growth and innovation. <https://www.photonics21.org/aboutus/photonics21.php>. Accessed 03 Jun 2022
2. Helmut H, Thomas G (2009) Laser in der Fertigung. Strahlquellen, Systeme, Fertigungsverfahren. Vieweg+Teubner Verlag | Springer Fachmedien Wiesbaden GmbH; Wiesbaden: Computer Science and Engineering (German Language). <https://doi.org/10.1007/978-3-8348-9570-7>
3. Poprawe R (2005) Lasertechnik für die Fertigung: Grundlagen, Perspektiven und Beispiele für den innovativen Ingenieur ; mit 26 Tabellen. VDI-Buch. Springer, Berlin, Heidelberg
4. Wang L, Zhang Y, Chia HY et al. (2022) Mechanism of keyhole pore formation in metal additive manufacturing. *npj Comput Mater* 8. <https://doi.org/10.1038/S41524-022-00699-6>
5. Huang Y, Fleming TG, Clark SJ et al (2022) Keyhole fluctuation and pore formation mechanisms during laser powder bed fusion additive manufacturing. *Nat Commun* 13:1170. <https://doi.org/10.1038/S41467-022-28694-X>
6. Bayat M, Thanki A, Mohanty S et al (2019) Keyhole-induced porosities in laser-based powder bed fusion (L-PBF) of Ti6Al4V: high-fidelity modelling and experimental validation. *Addit Manuf* 30:100835. <https://doi.org/10.1016/j.addma.2019.100835>
7. Tenbrock C, Fischer FG, Wissenbach K et al (2020) Influence of keyhole and conduction mode melting for top-hat shaped beam profiles in laser powder bed fusion. *J Mater Process Technol* 278:116514. <https://doi.org/10.1016/j.jmatprotec.2019.116514>
8. Gan Z, Kafka OL, Parab N et al (2021) Universal scaling laws of keyhole stability and porosity in 3D printing of metals. *Nat Commun* 12:2379. <https://doi.org/10.1038/s41467-021-22704-0>
9. Helm J, Schulz A, Olowinsky A et al (2020) Laser welding of laser-structured copper connectors for battery applications and power electronics. *Weld World* 64:611–622. <https://doi.org/10.1007/s40194-020-00849-8>
10. Fabbro R (2020) Depth Dependence and keyhole stability at threshold, for different laser welding regimes. *Appl Sci* 10:1487. <https://doi.org/10.3390/app10041487>
11. Grünewald J, Gehringer F, Schmöller M et al (2021) Influence of ring-shaped beam profiles on process stability and productivity in laser-based powder bed fusion of AISI 316L. *Metals* 11:1989. <https://doi.org/10.3390/met11121989>
12. McCann R, Obeidi MA, Hughes C et al (2021) In-situ sensing, process monitoring and machine control in laser powder bed fusion: a review. *Addit Manuf* 45:102058. <https://doi.org/10.1016/J.ADDMA.2021.102058>
13. You DY, Gao XD, Katayama S (2014) Review of laser welding monitoring. *Sci Technol Weld Joining* 19:181–201. <https://doi.org/10.1179/1362171813Y.0000000180>
14. Shi B, Chen Z (2021) A layer-wise multi-defect detection system for powder bed monitoring: lighting strategy for imaging, adaptive segmentation and classification. *Mater Des* 210:110035. <https://doi.org/10.1016/j.matdes.2021.110035>
15. Schmidt L, Römer F, Böttger D et al (2020) Acoustic process monitoring in laser beam welding. *Procedia CIRP* 94:763–768. <https://doi.org/10.1016/j.procir.2020.09.139>
16. Du Plessis A, Yadroitsev I, Yadroitsava I et al (2018) X-ray microcomputed tomography in additive manufacturing: a review of the current technology and applications. *3D Print Addit Manuf* 5:227–247. <https://doi.org/10.1089/3dp.2018.0060>
17. Gutknecht K, Cloots M, Sommerhuber R et al (2021) Mutual comparison of acoustic, pyrometric and thermographic laser powder

- bed fusion monitoring. *Mater Des* 210:110036. <https://doi.org/10.1016/j.matdes.2021.110036>
18. Czink S, Dietrich S, Schulze V (2022) Ultrasonic evaluation of elastic properties in laser powder bed fusion manufactured AlSi10Mg components. *NDT & E International* 132:102729. <https://doi.org/10.1016/j.ndteint.2022.102729>
 19. Norris JT, Robino CV (2008) Development of a time resolved energy absorption measurement technique for laser beam spot welds. In: International Congress on Applications of Lasers & Electro-Optics. Laser Institute of America, P149
 20. Simonds BJ, Sowards JW, Hadler J et al (2018) Dynamic and absolute measurements of laser coupling efficiency during laser spot welds. *Procedia CIRP* 74:632–635. <https://doi.org/10.1016/j.procir.2018.08.065>
 21. Simonds BJ, Sowards J, Hadler J et al (2018) Time-resolved absorptance and melt pool dynamics during intense laser irradiation of a metal. *Phys Rev Applied* 10:44061. <https://doi.org/10.1103/PhysRevApplied.10.044061>
 22. Bergström D, Kaplan A, Powell J (2005) Laser absorption measurements in opaque solids, in 10th NOLAMP Conference : the 10th Nordic Laser Materials Processing Conference Luleå Sweden, 49:444.
 23. Allen TR, Huang W, Tanner JR et al (2020) Energy-coupling mechanisms revealed through simultaneous keyhole depth and absorptance measurements during laser-metal processing. *Phys Rev Applied* 13:64070. <https://doi.org/10.1103/PhysRevApplied.13.064070>
 24. Simonds BJ, Garboczi EJ, Palmer TA et al (2020) Dynamic laser absorptance measured in a geometrically characterized stainless-steel powder layer. *Phys Rev Applied* 13:24057. <https://doi.org/10.1103/PhysRevApplied.13.024057>
 25. Trapp J, Rubenchik AM, Guss G et al (2017) In situ absorptivity measurements of metallic powders during laser powder-bed fusion additive manufacturing. *Appl Mater Today* 9:341–349. <https://doi.org/10.1016/j.apmt.2017.08.006>
 26. Simonds BJ, Tanner J, Artusio-Glimpse A et al (2020) Simultaneous high-speed x-ray transmission imaging and absolute dynamic absorptance measurements during high-power laser-metal processing. *Procedia CIRP* 94:775–779. <https://doi.org/10.1016/j.procir.2020.09.135>
 27. Simonds BJ, Tanner J, Artusio-Glimpse A et al (2021) The causal relationship between melt pool geometry and energy absorption measured in real time during laser-based manufacturing. *Appl Mater Today* 23:101049. <https://doi.org/10.1016/j.apmt.2021.101049>
 28. Yang L, Lo L, Ding S et al (2020) Monitoring and detection of melt pool and spatter regions in laser powder bed fusion of super alloy Inconel 625. *Prog Addit Manuf* 5:367–378. <https://doi.org/10.1007/s40964-020-00140-8>
- Publisher's note** Springer Nature remains neutral with regard to jurisdictional claims in published maps and institutional affiliations.